Article

Magnetism and charge density wave order in kagome FeGe

Xiaokun Teng [1,10], Ji Seop Oh [1,2,10], Hengxin Tan[3], Lebing Chen[1], Jianwei Huang [1], Bin Gao [1], Jia-Xin Yin [4], Jiun-Haw Chu [5], Makoto Hashimoto [6], Donghui Lu [6], Chris Jozwiak [7], Aaron Bostwick [7], Eli Rotenberg [7], Garrett E. Granroth [8], Binghai Yan [3], Robert J. Birgeneau [2,9] ✉, Pengcheng Dai[1] ✉ & Ming Yi [1] ✉

Electron correlations often lead to emergent orders in quantum materials, and one example is the kagome lattice materials where topological states exist in the presence of strong correlations between electrons. This arises from the features of the electronic band structure that are associated with the kagome lattice geometry: flat bands induced by destructive interference of the electronic wavefunctions, topological Dirac crossings and a pair of van Hove singularities. Various correlated electronic phases have been discovered in kagome lattice materials, including magnetism, charge density waves, nematicity and superconductivity. Recently, a charge density wave was discovered in the magnetic kagome FeGe, providing a platform for understanding the interplay between charge order and magnetism in kagome materials. Here we observe all three electronic signatures of the kagome lattice in FeGe using angle-resolved photoemission spectroscopy. The presence of van Hove singularities near the Fermi level is driven by the underlying magnetic exchange splitting. Furthermore, we show spectral evidence for the charge density wave as gaps near the Fermi level. Our observations point to the magnetic interaction-driven band modification resulting in the formation of the charge density wave and indicate an intertwined connection between the emergent magnetism and charge order in this moderately correlated kagome metal.

In quantum materials where the energy scale of electron–electron correlations is comparable to that of the electronic kinetic energy, a range of emergent electronic phases are found[1]. Well-known systems that exhibit such rich phase diagrams include the unconventional superconductor families of cuprates[2] and iron-based superconductors[3,4], where magnetic order, charge density wave (CDW) order, nematicity and superconductivity have been found in close proximity due to the entwinement of a multitude of degrees of freedom with similar energy scales, including spin, charge and orbitals. Besides engendering large quantum fluctuations that may give rise to novel phases, the intertwinement of multiple orders allows tunability of the ground state via the coupled order parameters. It is expected that, when quantum topology

---

[1]Department of Physics and Astronomy, Rice University, Houston, TX, USA. [2]Department of Physics, University of California, Berkeley, CA, USA. [3]Department of Condensed Matter Physics, Weizmann Institute of Science, Rehovot, Israel. [4]Department of Physics, Southern University of Science and Technology, Shenzhen, China. [5]Department of Physics, University of Washington, Seattle, WA, USA. [6]Stanford Synchrotron Radiation Lightsource, SLAC National Accelerator Laboratory, Menlo Park, CA, USA. [7]Advanced Light Source, Lawrence Berkeley National Laboratory, Berkeley, CA, USA. [8]Neutron Scattering Division, Oak Ridge National Laboratory, Oak Ridge, TN, USA. [9]Materials Science Division, Lawrence Berkeley National Laboratory, Berkeley, CA, USA. [10]These authors contributed equally: Xiaokun Teng, Ji Seop Oh. ✉e-mail: robertjb@berkeley.edu; pdai@rice.edu; mingyi@rice.edu

is realized in such a strongly correlated regime, unprecedented exotic phases are to be discovered. Recently, kagome lattices have been extensively investigated for the rich emergent physics associated with its lattice geometry in the presence of topology[5–19]. Among the insulators, quantum spin liquid states may exist due to the magnetic frustration[20]. Analogously, the geometric frustration for an electronic state could also cause localization as a way to quench the kinetic energy, thereby leading to a regime with narrow electronic bandwidth where electron correlation effects could be strong enough to induce emergent phases[5,6]. Equally importantly, the point group of the kagome lattice is that of graphene, hence the kagome lattice also shares many properties of the Dirac fermions. Therefore, kagome lattices have been intensely explored as a model system to realize topology in the presence of strong electron correlations.

Among the known kagome metals, some exhibit magnetic order with ferromagnetically ordered sheets that are either ferromagnetically or antiferromagnetically stacked[8–15], with ordering temperatures often exceeding room temperature. Another class of recently discovered kagome materials, AV$_3$Sb$_5$ (A = K, Rb, Cs)[17–19], hosts CDW order near 100 K that may be associated with time-reversal symmetry-breaking[21,22]. The interpretation on the origin of these orders ranges from those initiated from a strongly interacting picture to those based on electronic instabilities from band structure[23–28]. For a two-dimensional (2D) kagome lattice, three key features have been identified in the electronic structure (Fig. 1d): (1) a flat band derived from the destructive interference, (2) a Dirac crossing at the Brillouin zone (BZ) corner (K point in the inset of Fig. 1d) and (3) a pair of Van Hove singularities (VHSs) at the BZ boundary (M point). It has been proposed that the large density of states (DOS) from the kagome flat bands could induce ferromagnetism[5]. Alternatively, at special fillings where the VHS is at the Fermi level (E_F), interaction between the saddle points could also induce CDW order[6,25–27]. The large energy separation between the flat band and the VHSs (Fig. 1d,e) may be one reason why CDW order and magnetic order have not been commonly observed simultaneously within one system. Efforts at tuning the ordered phases include tuning the energy location of either the flat bands or VHSs relative to the chemical potential via chemical doping[29], hydrostatic pressure[30] and uniaxial strain[31], all of which have demonstrated potential yet so far have resulted in decoupled order parameters of either magnetism or CDW order.

Very recently, it was discovered that CDW order appears deep in a magnetically ordered kagome metal (FeGe)[32,33], providing the opportunity to explore the possible connection between magnetism and CDW order on a kagome lattice. Hexagonal FeGe (refs. [34,35]) (Fig. 1a,b), which is isostructural to FeSn and CoSn, consists of stacks of Fe kagome planes with both in-plane and inter-plane Ge atoms. A sequence of phase transitions has been found (Fig. 1c). First, an A-type antiferromagnetic (AFM) order appears below a Néel temperature $T_N \approx 410$ K, with moments aligned ferromagnetically along the c axis within each plane and anti-aligned between layers (Fig. 1a). At 100 K, where CDW order takes place (T_{CDW}), two types of CDW order were found with $\mathbf{Q}_{CDW1} = (0.5, 0, 0)/(0, 0.5, 0)$, that is, completely in-plane, and $\mathbf{Q}_{CDW2} = (0.5, 0, 0.5)/(0, 0.5, 0.5)$, which also has an out-of-plane component, similar to that found in the AV$_3$Sb$_5$ systems[17]. Finally, at a lower temperature of $T_{canting} \approx 60$ K, the magnetic moments cant from the c direction to give a c axis double cone (canted) AFM structure. In addition, evidence of strong coupling between the CDW order and AFM order has been reported in the form of an enhanced magnetic moment at the onset of the CDW order[32].

Here, we use a combination of high-resolution angle-resolved photoemission spectroscopy (ARPES), inelastic neutron scattering (INS) and density functional theory (DFT) to study the formation of the CDW order from the magnetic phase to gain insights into the potential contributors to the origin of CDW order in magnetic FeGe. In particular, in the AFM state, we observe saddle points in the vicinity of E_F, as

well as kagome flat bands and Dirac cones (DCs). With the guidance of DFT calculations, we identify an orbital-selective contribution of VHS to a potential nesting condition near E_F, enabled by the spin splitting of the bands within each ferromagnetic (FM) kagome layer. At T_{CDW}, gaps open on the VHS bands across the $\mathbf{Q}_{CDW}$ vectors. In addition, we find that the electronic states on the VHS bands couple to an optical phonon mode. We therefore identify the key ingredients for the formation of CDW in kagome FeGe to be the presence of orbital-selective VHS near E_F induced by the spin splitting of the ordered moment as well as electron–phonon coupling. The observations taken together suggest an intimate connection between the CDW order and magnetism on the kagome lattice and lay the groundwork for theoretical efforts incorporating electron correlations to identify CDW order formation in a magnetic kagome lattice.

We begin with an overview of the electronic structure of FeGe from DFT calculations. Consistent with previous first-principle calculations[36–38], the DOS calculated for the paramagnetic (PM) phase exhibit a large peak at E_F, which splits into two in the AFM phase (Fig. 1f). By directly comparing with the band structures calculated in each phase (Fig. 1e), the peaks in the DOS are indeed associated with the kagome flat bands. Moreover, although the magnetic structure in FeGe is AFM, each kagome layer is FM with a well-defined spin-majority and spin-minority contribution. From Fig. 1e, we confirm that the flat bands above E_F in the AFM phase correspond to the spin-minority bands while those below E_F correspond to the spin-majority bands within each FM layer. Hence, one can largely interpret the AFM band structures as an interaction-driven magnetic splitting of the kagome bands within each FM layer (Fig. 1d). Interestingly, the consequence of such splitting is that the VHSs that were relatively far from E_F in the PM state are brought to the vicinity of E_F in the AFM phase in the spin-minority sector, as shown by the marked VHS1 and VHS2 in Fig. 1e. Although DFT cannot capture all the details of the experimental observations because this is a moderately correlated system, we will show in the following that this qualitative understanding is consistent with our experimental observations.

Next, we gauge the strength of the electron correlations in FeGe by comparing the measured DOS with DFT. From our angle-integrated photoemission spectrum, we can identify key spectral features that match with those from the calculated DOS in the AFM phase (Supplementary Fig. S1), which allows us to extract an overall renormalization factor of 1.6, close to that in some of the iron-based superconductors[4]. With such a renormalization factor, the DFT calculated band structure for the AFM state can provide a reasonable match with that of the measured dispersions covered in a large energy range (Fig. 2c). In particular, we can identify a broad band near −0.75 eV that matches the location of the spin-majority kagome flat bands. Next, we examine the key signatures of the kagome electronic structure near E_F in the AFM phase. From a detailed photon energy measurement, we identify 69 eV photons to cross the $k_z = 0$ plane while 47 and 102 eV photons to cross the $k_z = \pi$ plane (Supplementary Fig. S3). Since the photoemission process is subject to a substantial k_z broadening effect[39], we discuss the following using the 2D projected notation of the BZ (Fig. 2a). We find two types of terminations among the samples measured, corresponding to the Ge and Fe kagome terminations, similar to the case of FeSn (ref. [9]). From a detailed analysis of the two terminations (Supplementary Figs. S2, S3, S4 and S6), we can identify two sets of VHSs and DCs that are termination independent and therefore intrinsic to the bulk kagome layers. The first set (marked in blue as VHS1 and DC1) consists of linear bands that cross at −0.6 eV at the BZ corner, $\bar{K}$ points (Fig. 2d). The DC structures can be better visualized in a stack of constant energy contour plots in Fig. 2e, where circular contours shrink down to the Dirac point and expand out again. Furthermore, the linear dispersions from DC1 rise to cross E_F, forming a VHS on the BZ edge, $\bar{M}$ point (Fig. 2d,e). The saddle point nature of this VHS can be better visualized from a series of cuts across the $\bar{M}$ point (Fig. 2f), where the band top of
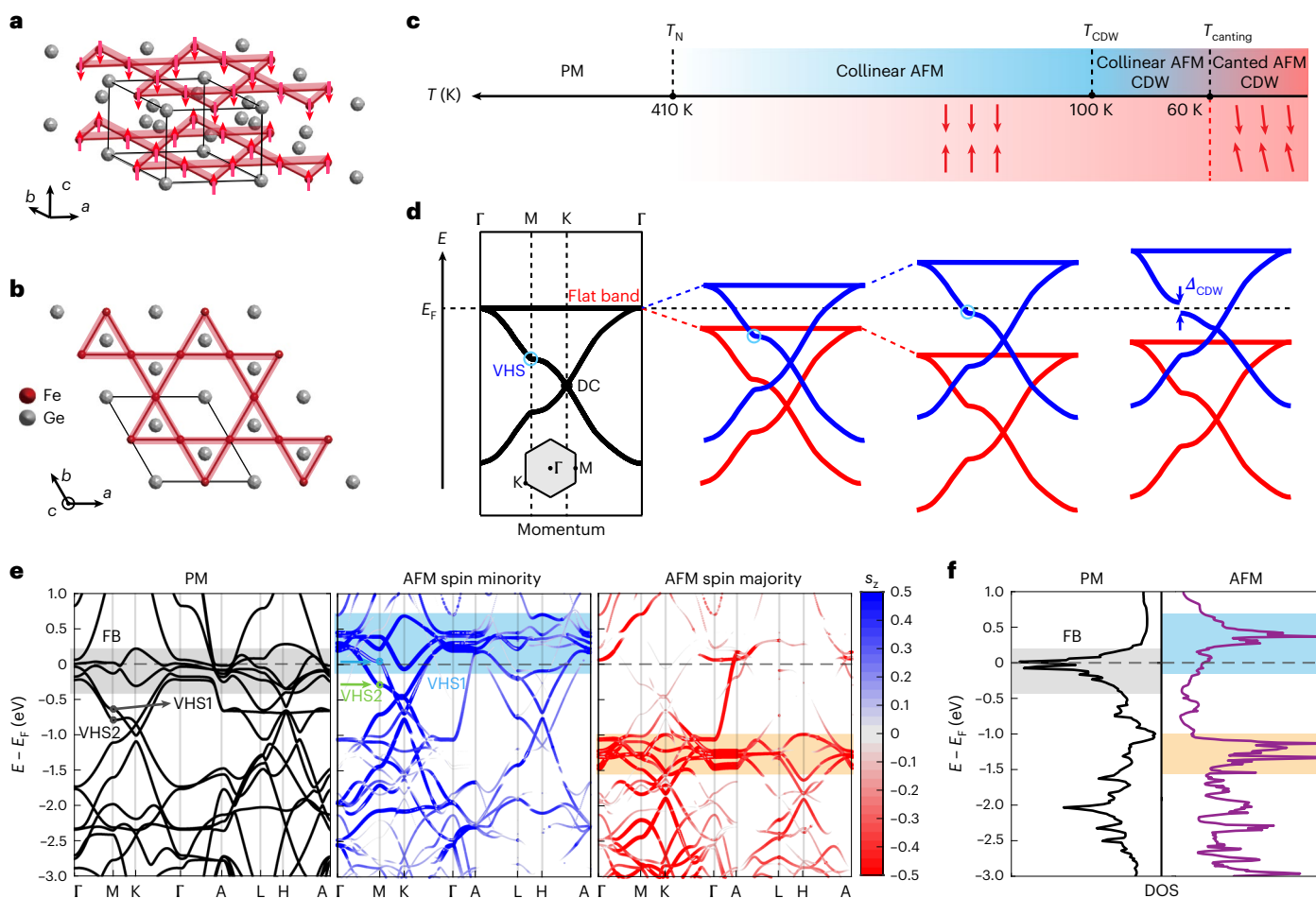
Fig. 1 | Crystal structure and electronic structure. a, The crystal structure of hexagonal FeGe with the unit cell shown by solid lines. Fe atoms are labelled in red and Ge atoms in grey. A-type AFM order is illustrated by red arrows denoting spin ordering of Fe atoms. **b**, A top view of the crystal structure to visualize the Fe kagome layer. **c**, A summary of the transitions as a function of temperature. **d**, A simplified schematic summary of AFM-induced band splitting plotted in energy (E) versus momentum. In the PM state, the kagome flat band appears at E_F, with a Dirac crossing and a pair of VHSs well below E_F. In the AFM phase, the ordered moment within each ferromagnetic layer induces exchange splitting of the spin-minority and spin-majority bands, resulting in an upshift of the blue VHS towards E_F. At the onset of CDW order, a gap (Δ_{CDW}) opens at the VHS band near E_F. The temperature evolution (horizontal direction) is aligned with the temperature axis in **c. e**, DFT calculated band structures for the PM state, as well as those for the spin-minority and spin-majority bands within an FM layer in the AFM state. Colour indicates the spin projection (s_z). Flat band (FB) regions are highlighted with coloured shades. **f**, DOS calculations for the PM and AFM phases.

the hole-like band parallel to $\bar{K}-\bar{M}-\bar{K}$ has a minimum energy at the $\bar{M}$ point, indicative of the electron-like nature in the orthogonal direction. The Fermi momenta (k_F) of this VHS1 (denoted by blue dots) form circular Fermi pockets (Fig. 2e). Besides this set of DC and VHS, a second set (labelled in dark green) consists of a DC2 at −0.2 eV that is connected to VHS2 slightly below E_F with a much smaller band velocity compared with that of VHS1. In addition, we also identify a DC3 at −0.06 eV. For the hexagonal lattice symmetry, the five Fe 3d orbitals are split into three groups: $d_{x^2-y^2}/d_{xy}$, d_{xz}/d_{yz} and d_{z^2}. Guided by orbital-projected DFT calculations and consideration of both in-plane and out-of-plane band velocities (Supplementary Figs. S4 and S5), we identify DC1/VHS1 to be of $d_{x^2-y^2}/d_{xy}$ origin, DC2/VHS2 to be of d_{xz}/d_{yz} origin and DC3 to be of d_{z^2} origin. A summary of the identified VHSs and DCs is shown in Fig. 2b. We note that, while common features can be identified between DFT and measured dispersions, the precise locations of the VHSs are not well captured by DFT even with the overall renormalization, suggesting non-negligible correlation effects at play.

If the qualitative understanding of the spin splitting from DFT calculations is correct, the VHSs near E_F observed in the AFM state must be the spin-minority set that is shifted up as the magnetic moment orders with lowering temperature. To check for this, we examine the

temperature evolution of VHS1, which as a mostly in-plane orbital can be tracked more accurately as it is less affected by k_z broadening compared with VHS2. Figure 3e shows the spectral images of the VHS1 at 11 K and 260 K. The VHS point visibly shifts in energy as temperature is varied, as also seen in the extracted momentum distribution curves (MDCs) from −0.04 eV as a function of temperature (Fig. 3f). The peak from the VHS band is observed to shift away from the M point as temperature is lowered, consistent with the shifting-up behaviour of the VHS (Fig. 3h). We can further extract the energy location of the VHS. In Fig. 3a, we identify the bands leading to VHS1. Since the VHS point is slightly above E_F, to track its energy position, we first fit the band dispersion at each temperature from an MDC analysis. From the MDC, we identify a main peak next to another feature in the form of a smaller peak. We fit the MDC line profile to two Lorentzian functions on a Gaussian background. The location of the VHS band can therefore be extracted as a function of binding energy (Fig. 3d). We then fit for the location of the band top using a parabolic function of the dispersion at each temperature. We note that only the dispersion lower than −30 meV is used in the parabolic fit to avoid any complication due to the potential opening of a CDW gap or dispersion kink. The extracted location of VHS1 is plotted as a function of temperature in Fig. 3h, showing
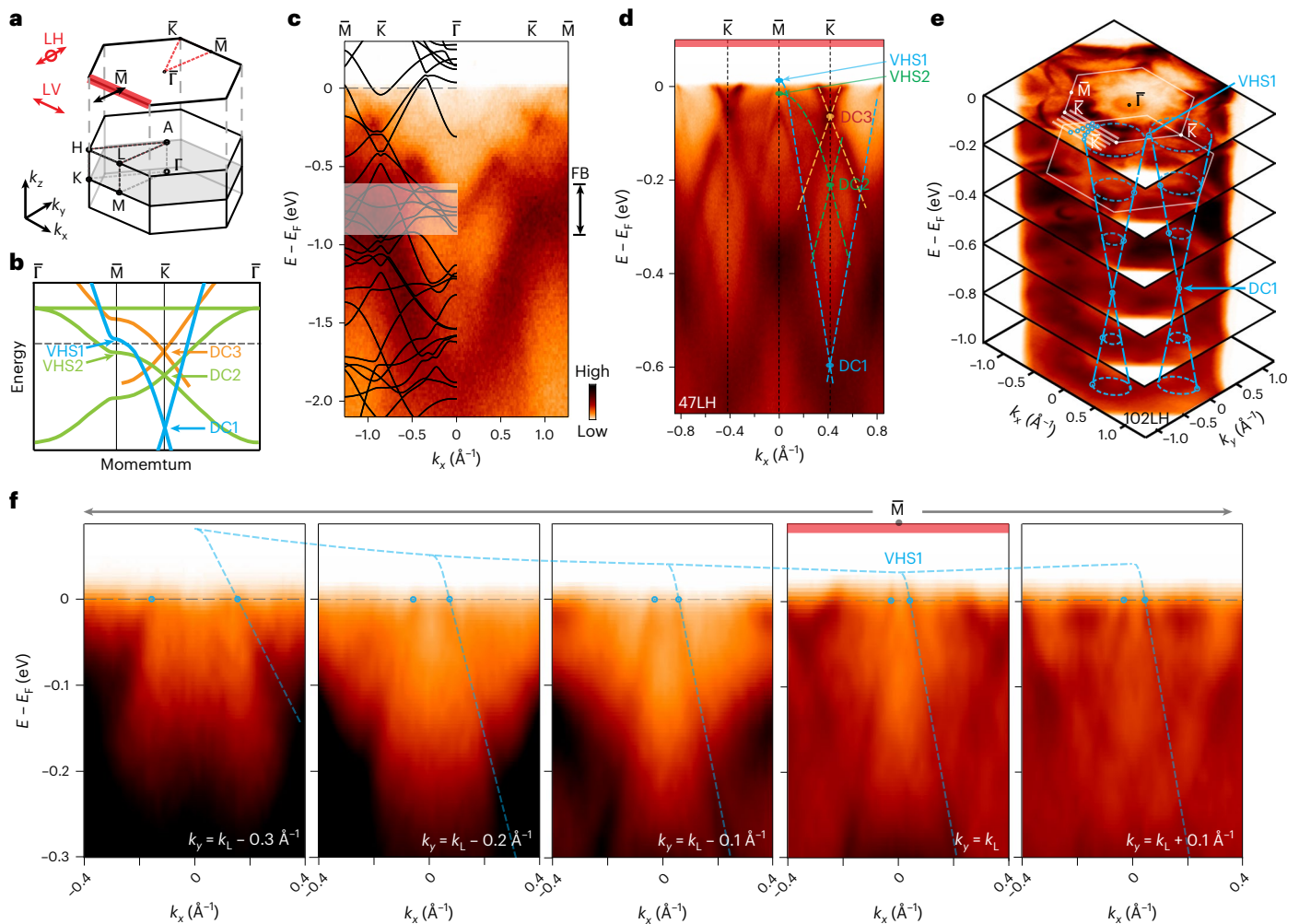
Fig. 2 | Key signatures of kagome band structure. a, 3D and 2D projected BZ notations with polarization vectors indicated. **b**, Schematic of DCs and associated VHSs. **c**, Large energy range dispersions measured compared with that from DFT calculation after renormalization by a factor of 1.6. The lower kagome flat bands are highlighted similarly to in Fig. 1e. **d**, Spectral image measured along $\bar{K} - \bar{M} - \bar{K}$ using LH 47 eV photons. **e**, Constant energy contours measured with 102 eV photons and LH polarization. Dashed blue lines indicate a DC at the $\bar{K}$ point and the corresponding VHS at $\bar{M}$. **f**, Stack of cuts taken along k_x at $k_y = k_L - 0.3$ Å^{-1}, $k_L - 0.2$ Å^{-1}, $k_L - 0.1$ Å^{-1}, k_L and $k_L + 0.1$ Å^{-1}, as indicated in **e** as solid white lines. Thick red lines at the top of **d** and fourth figure in **f** indicate they are the high symmetry cuts, as illustrated in **a**. The Fermi crossings are marked by blue dots, also marked on the corresponding cuts in **e**. All data are taken at 11 K.

an upward shift as temperature is lowered towards T_{CDW}. Additional evidence for the band shift is seen in the peak shift from both energy distribution curves (EDCs) and MDCs as a function of temperature (Supplementary Fig. S7). The trend of the shift is consistent with the ordering of the magnetic moment (m), as can be seen by overlaying in Fig. 3g the m^2 measured from neutron diffraction[32].

As the VHSs are shifted to the vicinity of E_F by the magnetic order, we therefore examine the potential role of the VHSs in the formation of the CDW order. At 140 K above the onset of the CDW order, VHS1 is above E_F while VHS2 is below E_F. They form distinct Fermi surfaces. In particular, the Fermi surface from VHS1 (xy/x^2-y^2) can be better observed under an in-plane polarization (linear vertical, LV) while VHS2 (xz/yz) can be better observed in the linear horizontal (LH) polarization that contains an out-of-plane component (Fig. 4a). Noticeably, the VHS1 band forms a circular Fermi surface, while that of the VHS2 band resembles more that of the triangular Fermi surface predicted by kagome models at VHS filling[6]. We can further confirm their contribution to the potential nesting condition using DFT-based Lindhard susceptibility calculations (Supplementary Fig. S11). While DFT does not accurately reproduce the Fermi surface, the chemical potential can be tuned to identify energies where such Fermi surface contours are

revealed. A susceptibility calculation at such energy that reproduces the VHS2 fermiology indeed produces a peak at the 2×2 CDW wavevector, while that done for the VHS1 fermiology does not (Supplementary Fig. S11). This suggests that the VHS contribution to the CDW formation may be orbital dependent in FeGe, as has also been reported for CsV_3Sb_5 (ref. [40]).

Furthermore, we can identify participation of the VHS bands in the CDW ordering by comparing the band dispersions across T_{CDW}. From a comparison of the Fermi surface at 140 and 13 K (Fig. 4a,b), we see that the VHS2 undergoes the largest change as evident in the increased curvature of its Fermi pocket. This can also be seen by comparing two cuts across T_{CDW}. On the cut along $\bar{K} - \bar{M} - \bar{K}$ (Fig. 4c,d), even though matrix elements suppress the spectral weight of VHS2, we can still identify the presence of k_z broadened VHS2 via a hump in the EDC (Fig. 4g). In the CDW phase, an additional peak appears close to E_F in the EDC (Fig. 4g), consistent with the splitting of the band (Supplementary Fig. S9). Such band splitting at the M point is reminiscent to that observed in CsV_3Sb_5 (ref. [40]) and is interpreted to be the result of folding and gap opening at the M point. On a parallel cut away from $\bar{K} - \bar{M} - \bar{K}$, gap opening can also be observed on VHS2 with a typical bend-back behaviour of the dispersion (Fig. 4e,f,h and Supplementary Fig. S9).
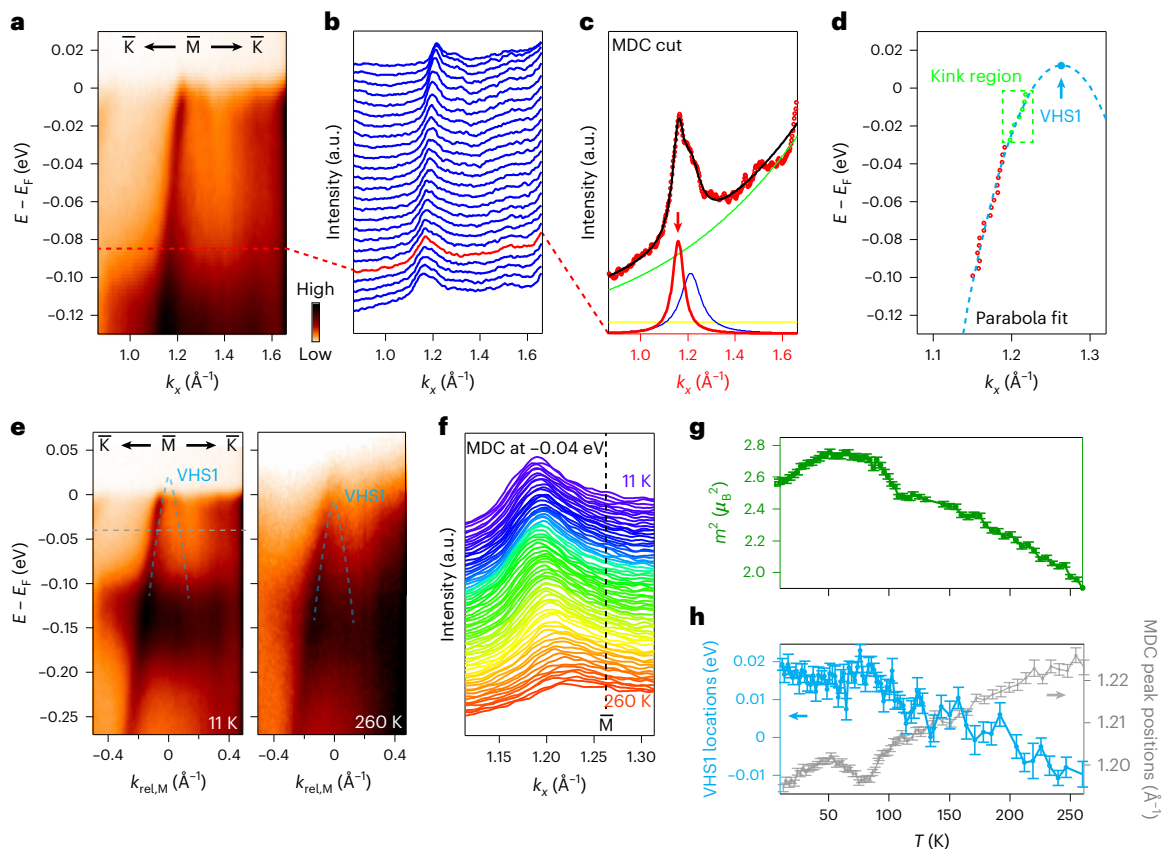
Fig. 3 | Temperature evolution of VHS. a, Spectral images across the $\bar{M}$ point along $\bar{K} - \bar{M} - \bar{K}$, taken with LH-polarized 69 eV photons. **b**, A stack of MDCs (from E_F to −0.1 eV) from **a**. The red line in the stack is the MDC curve along the dashed red line in **a**. **c**, The MDC from the red dashed line in **a** (identical to the red curve in **b**). We fit the curve with two Lorentzians (red and blue), one background Gaussian profile (light green) and a constant background (yellow) curve. **d**, Fitting results from the MDC stack. Red circles are peak positions of VHS1-forming band dispersions (red curve in **b**). We use a parabolic fit to extrapolate locations of VHS1 above E_F. **e**, Spectral images across the $\bar{M}$ point along $\bar{K} - \bar{M} - \bar{K}$, showing the temperature evolution of VHS1. **f**, MDCs taken at the dashed grey line in **e**, measured as a function of temperature. **g**, The ordered magnetic moment measured by neutron scattering, reproduced from ref. [20] (green). **h**, Extracted VHS1 locations (blue) and the fitted peaks in MDC taken from **f** (grey). Error bars are from the s.d. resulting from the fitting process.

Besides VHS2, we also observe spectral gap opening on VHS1. Spectral images across the $\bar{K} - \bar{M} - \bar{K}$ cut are shown for 140 K > T_{CDW} (Fig. 4i, left side) and 70 K < T_{CDW} (Fig. 4i, right side). The spectra have been divided by the Fermi–Dirac function convolved with the instrument resolution to also uncover spectral weight above E_F. Noticeably, a spectral weight suppression is observed on VHS1, not on any other bands crossing E_F. This is further confirmed by the EDC for the VHS1 at k_{VHS}, where a spectral weight suppression below T_{CDW} indicates the gap opening (Fig. 4j and Supplementary Fig. S8). The observable lower edge of the gap below E_F is −20 meV, consistent with the observed full gap size of 50 meV by scanning tunnelling microscopy[33]. In contrast, the EDCs for the other band crossings away from the BZ edge, L points in the CDW ordered phase show ungapped peaks at E_F in the CDW phase, indicating that the CDW gap is momentum dependent. Figure 4k shows a continuous temperature evolution of the symmetrized EDC taken at k_{VHS}, where a gap appears below T_{CDW}. The integrated spectral weight within the gap energy of 20 meV of E_F is shown in Fig. 4l, where the smoothed average of the scattered data points (Fig. 4l, red line) shows a trend consistent with the onset of the depletion of the spectral weight at T_{CDW} = 100 K (Supplementary Fig. S8).

Lastly, we report on the observation of electron–phonon coupling in FeGe. Dispersion kinks have been reported in unconventional superconductors such as the cuprates and iron-based superconductors[2,3,39,41,42]. The origin of such dispersion kinks has been proposed to indicate electron–boson coupling, to either phonons or magnons. On the VHS1 band where a CDW gap is observed, a kink structure is observed in the electronic dispersion (Fig. 5a). We can use MDC analysis to extract the real and imaginary parts of the self-energy from the peak position and the full-width at half-maximum of the MDC fitting, respectively (Fig. 5b–d), showing the coupling of the electrons to a bosonic mode at around 30 meV below E_F. We can then extract an electron–boson coupling constant from the slope of the real part of the self-energy as well as from the ratio of the renormalized band velocity (v_F) and the bare-band velocity (v_{F0}), both of which give a consistent coupling constant λ of approximately 0.5–0.6 (refs. [43,44]). Notably, this kink structure has little resolvable temperature dependence from 11 K ($T < T_{canting}$) to 70 K ($T_{canting} < T < T_{CDW}$) to 140 K ($T_{CDW} < T$).

To identify the origin of this bosonic mode, we carried out INS measurements. As presented in Fig. 5f, the observed spin waves stemming from the AFM zone centre and in-plane Γ point cross the M point at 70 meV, far above the interaction point of 30 meV. Therefore, a direct electron–magnon interaction at the M point is ruled out. In contrast, the phonon spectra do reveal optical modes near 33–38 meV around the M point (Fig. 5e). More interestingly, a hardening of this optical phonon mode at 33 meV is observed across the T_{CDW} from 120 K to 70 K, appearing at the M point and extending to the K points (Fig. 5i and Supplementary Fig. S10b). Such hardening is absent at the Γ points (Fig. 5h). This optical phonon mode, therefore, is likely the mode responsible for the dispersion kink observed in ARPES measurements. We note that the size of the hardening is about 1 meV, which is too small to be resolved
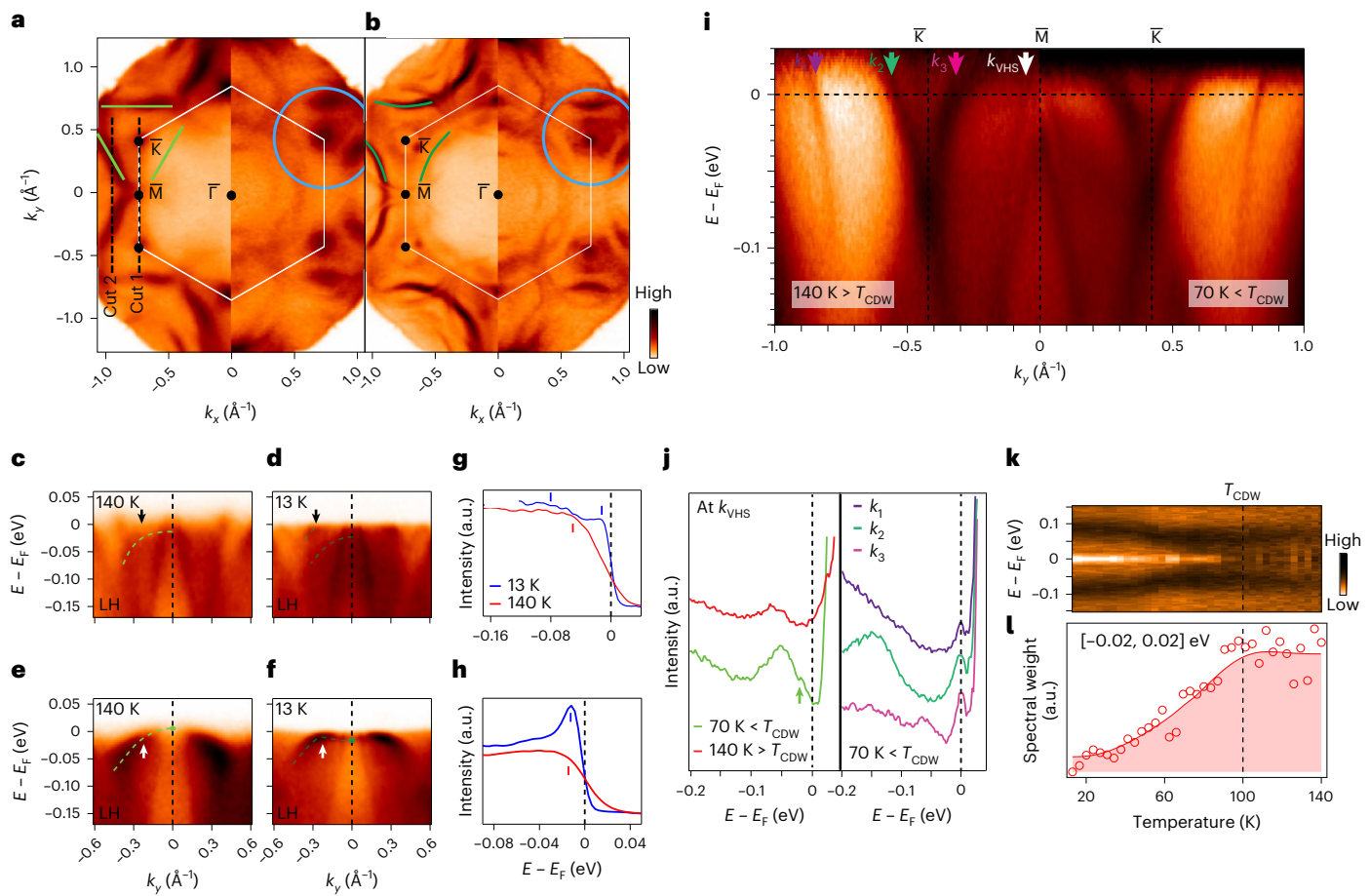
Fig. 4 | Observation of CDW gap. a, Fermi surface taken on kagome termination at 140 K with 69 eV photons, with the left half under LH polarization and the right half under LV polarization. **b**, The same as **a** but taken at 13 K. Blue and green lines/curves in **a** and **b** delineate the Fermi surfaces formed by VHS1 and VHS2, respectively, serving as guide to the eyes. **c**,**d**, $\bar{K}$–$\bar{M}$–$\bar{K}$ cut (cut 1) from **a** (**c**) and **b** (**d**). **e**,**f**, Cut 2 from **a** (**e**) and **b** (**f**), showing CDW gap opening on the VHS2 band. Green dashed lines in **c**–**f** indicate VHS2 bands. **g**, EDC from cut 1 marked by the arrow, showing the appearance of two features at 13 K. **h**, EDC from cut 2 marked by the arrow, showing the gap opening. **i**, Spectral image taken with LH-polarized 47 eV photons across the $\bar{K}$–$\bar{M}$–$\bar{K}$ high symmetry direction at 140 K > T_{CDW} (left)

and 70 K < T_{CDW} (right). The data have been divided by the Fermi–Dirac function convolved with the energy resolution to reveal signal above E_F. The Fermi momenta of four band dispersions are indicated (k_1, k_2, k_3 and k_{VHS}), where k_{VHS} corresponds to the VHS crossing. **j**, EDC at k_{VHS}, showing a gap below T_{CDW}, as well as EDCs for other band crossings as labelled in **i**, showing no gap opening. **k**, Temperature evolution of the symmetrized EDC taken at k_{VHS}. **l**, Integrated spectral weight across the CDW gap energy between [−0.02, 0.02] eV at k_{VHS} as a function of temperature (red circles). The red line is the smoothed average of the data points, showing a suppression onset at T_{CDW}.

in the temperature-dependent kink analysis (Fig. 5a). To identify the phonon mode, we carried out phonon calculations using DFT, which match excellently with the measured phonon spectra (Fig. 5e). The optical phonon is determined to be an A_{2u} mode involving the movement of the Fe atoms from the kagome plane as well as movement of the inter-layer Ge atoms (Fig. 5j). In addition, we observe no acoustic phonon softening from 8 K to 70 K (Supplementary Fig. S10a), contrary to the behaviour in the A_{2u} optical mode across the same temperature region. The electron–phonon coupling here in FeGe is similar in many aspects to that in the AV$_3$Sb$_5$ system, where a dispersion kink at a similar energy scale of 36 meV has also been reported[42]. In addition, a hardening of the B_{3u} longitudinal optical phonon mode around 10 meV has been observed in AV$_3$Sb$_5$ across its T_{CDW} (ref. [43]), while no acoustic phonon softening is observed[42,44].

Having presented all the data, we now discuss the implications. We have experimentally identified potential key ingredients for the formation of the CDW order in magnetic FeGe, namely the orbital-dependent VHSs that are brought to the vicinity of E_F due to the magnetic splitting of the bands. The contribution of the VHSs to the formation of the CDW order is evident in the opening of gaps at E_F in the CDW phase while other bands remain gapless. In addition, we identify

electron–phonon coupling around the M point of the BZ that is connected by the CDW wavevector. We can first compare the phenomenology of the CDW order in FeGe with that in non-magnetic kagome AV$_3$Sb$_5$ (refs. [17–19,30–32,42–50]). In both CDW ordered phases, VHSs are observed to be in the vicinity of E_F, albeit accidental in AV$_3$Sb$_5$ and magnetism assisted in FeGe. The VHSs are observed to have orbital-dependent contributions gauged from their fermiology. In both cases, the xz/yz orbitals are proposed to be dominant[45]. The CDW gap at E_F is observed at the BZ edge, which is connected by wavevectors that correspond to the diffraction peaks seen by X-rays and neutrons. Electron–phonon coupling is present in both systems in the absence of acoustic phonon softening at the CDW wavevectors[42–44]. These similarities point to a potential universality of the phenomenology of CDW among the kagome metals. However, the microscopic origin of the CDW order in kagome system is still unresolved. In the weakly correlated AV$_3$Sb$_5$ system, nesting of VHSs has been proposed based on 2D models. In FeGe, however, the moderate electron correlations deem a purely nesting-driven scenario unlikely. This is reflected in the larger degree of mismatch between DFT and measured dispersions in FeGe as well as the difficulty to stabilize a CDW order from DFT alone. If nesting is indeed the dominant driver, then it may be expected that other A-type AFM kagome systems, such
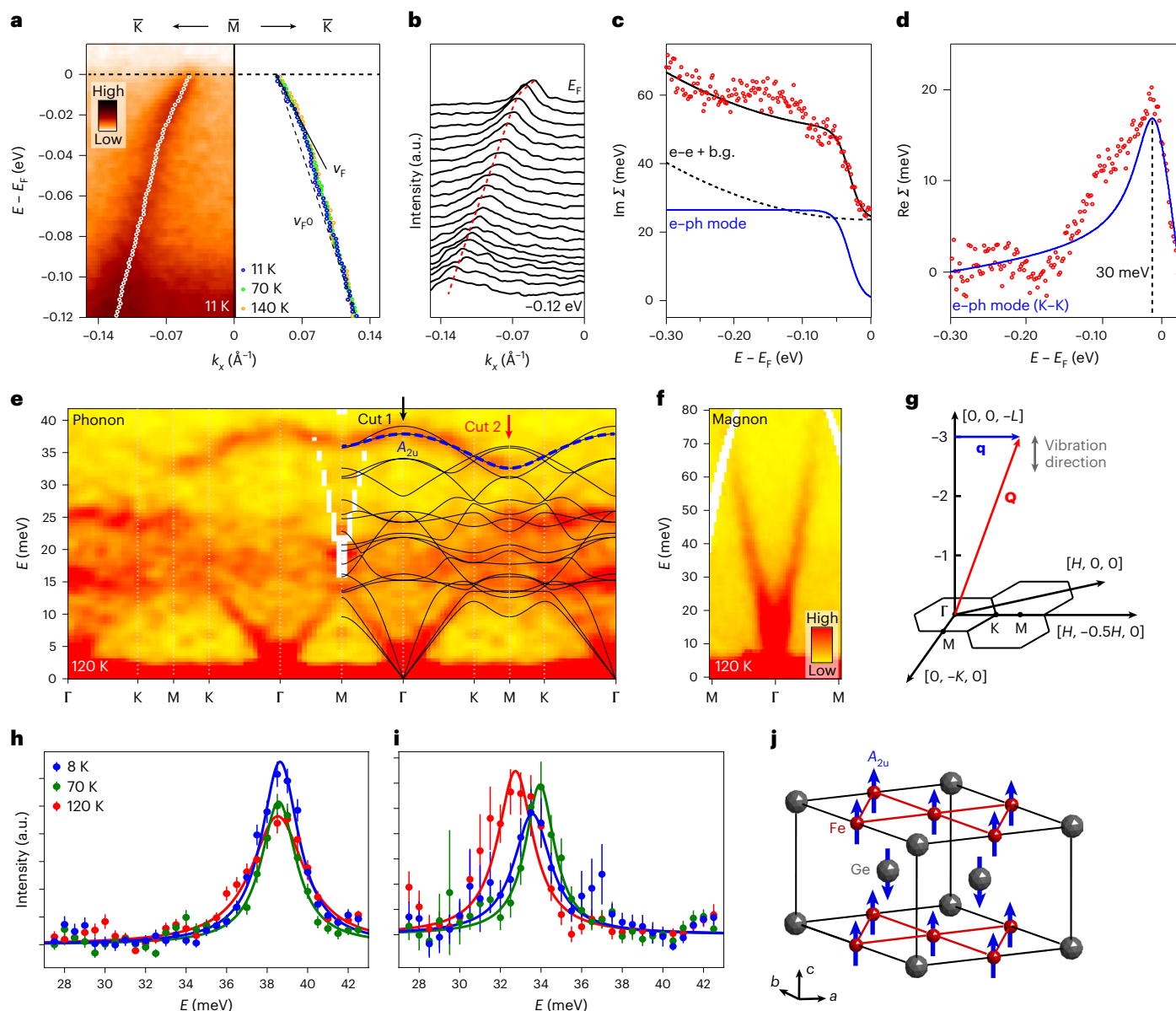
Fig. 5 | Electron–boson coupling in FeGe. a, VHS1-forming band dispersion (same one as in Fig. 3). White dots are fitted band dispersions from MDC analysis. On the right, MDC fitting results at 11 K ($T < T_{canting}$), 70 K ($T_{canting} < T < T_{CDW}$) and 140 K ($T_{CDW} < T$) are overlaid. **b**, A stack of MDCs directly visualizing the kink structure. **c**, The imaginary part of the self-energy derived from width analysis of MDC fittings. Σ denotes self-energy. We introduce one electron–phonon (e–ph) coupling mode together with background (b.g.) signals considering moderate electron–electron (e–e) interaction (Fermi-liquid-like behaviour). **d**, The real part of the self-energy analysis of peak position from MDC fittings. We overlay the Kramers–Kronig transformed electron–boson coupling mode from the imaginary part of the self-energy (solid blue curve in **c**). A bosonic mode is observed at 30 meV. **e**, INS measurement at 120 K of the in-plane phonon

spectra at $L = [−3.1, −2.9]$ with DFT calculated phonon spectra overlaid. **f**, INS measurement of the in-plane magnon spectra with $L = [−2.6, 0]$. The colour bar of **f** is same for **e**. **g**, INS measurement geometry illustrating the relationship between neutron momentum transfer **Q**, phonon wavevector **q** and vibrational direction. **h**, Measured phonon spectra at the Γ (0, 0, 3) point (cut 1), showing no temperature dependence. **i**, Measured phonon spectra at the M points (cut 2, averaged between (1, −0.5, 3) and (−1, 0.5, 3)), showing hardening of the optical phonon mode across T_{CDW}. In **h** and **i**, blue, green and red dots indicate 8 K, 70 K, 120 K data, respectively. Solid lines are fitting with a Lorentzian and a linear background. Error bars represent one s.d. The fitted energy at (8 K, 70 K, 120 K) is (32.74 ± 0.13 meV, 33.94 ± 0.10 meV, 33.57 ± 0.15 meV). The colour scheme for **h** is same for **i**. **j**, Identified phonon mode (A_{2u}) for the optical branch outlined in **e**.

as FeSn (ref. [9]), could also develop 2 × 2 CDW order when the spin split-ting shifts the VHSs at M into the proximity of E_F. Since FeGe is the only kagome lattice magnet with CDW discovered so far, it is therefore likely that correlation effects, perhaps even orbital-dependent correlation effects, must be taken into consideration in addition to the VHS presence near E_F to understand the origin of the CDW order in magnetic kagome systems. Regardless of the ultimate microscopic theoretical description of the CDW on stacked kagome lattices, our work reveals an intimate interaction of the CDW order and magnetism in a moderately correlated

kagome metal and provides experimental groundwork towards a potential universal understanding of CDW order in kagome systems.

Online content

Any methods, additional references, Nature Portfolio reporting summaries, source data, extended data, supplementary information, acknowledgements, peer review information; details of author contributions and competing interests; and statements of data and code availability are available at https://doi.org/10.1038/s41567-023-01985-w.

References

1. Paschen, S. & Si, Q. Quantum phases driven by strong correlations. *Nat. Rev. Phys.* **3**, 9–26 (2021).
2. Keimer, B. et al. From quantum matter to high-temperature superconductivity in copper oxides. *Nature* **518**, 179–186 (2015).
3. Fernandes, R. M. et al. Iron pnictides and chalcogenides: a new paradigm for superconductivity. *Nature* **601**, 35–44 (2022).
4. Yi, M., Zhang, Y., Shen, Z.-X. & Lu, D. Role of the orbital degree of freedom in iron-based superconductors. *npj Quantum Mater.* **2**, 57 (2017).
5. Mielke, A. Ferromagnetic ground states for the Hubbard model on line graphs. *J. Phys. A* **24**, L73 (1991).
6. Kiesel, M. L., Platt, C. & Thomale, R. Unconventional Fermi surface instabilities in the kagome Hubbard model. *Phys. Rev. Lett.* **110**, 126405 (2013).
7. Lin, Z. et al. Flatbands and emergent ferromagnetic ordering in Fe_3Sn_2 kagome lattices. *Phys. Rev. Lett.* **121**, 096401 (2018).
8. Ye, L. et al. Massive Dirac fermions in a ferromagnetic kagome metal. *Nature* **555**, 638–642 (2018).
9. Kang, M. et al. Dirac fermions and flat bands in the ideal kagome metal FeSn. *Nat. Mater.* **19**, 163–169 (2020).
10. Xie, Y. et al. Spin excitations in metallic kagome lattice FeSn and CoSn. *Commun. Phys.* **4**, 240 (2021).
11. Yin, J.-X. et al. Quantum-limit Chern topological magnetism in $TbMn_6Sn_6$. *Nature* **583**, 533–536 (2020).
12. Li, M. et al. Dirac cone, flat band and saddle point in kagome magnet YMn_6Sn_6. *Nat. Commun.* **12**, 3129 (2021).
13. Morali, Noam et al. Fermi-arc diversity on surface terminations of the magnetic Weyl semimetal $Co_3Sn_2S_2$. *Science* **365**, 1286–1291 (2019).
14. Liu, D. F. et al. Magnetic Weyl semimetal phase in a kagomé crystal. *Science* **365**, 1282–1285 (2019).
15. Wang, Q. et al. Field-induced topological Hall effect and double-fan spin structure with a *c*-axis component in the metallic kagome antiferromagnetic compound YMn_6Sn_6. *Phys. Rev. B* **103**, 014416 (2021).
16. Yin, J.-X. et al. Negative flat band magnetism in a spin–orbit-coupled correlated kagome magnet. *Nat. Phys.* **15**, 443–448 (2019).
17. Ortiz, B. R. et al. CsV_3Sb_5: a Z_2 topological kagome metal with a superconducting ground state. *Phys. Rev. Lett.* **125**, 247002 (2020).
18. Zhao, H. et al. Cascade of correlated electron states in the kagome superconductor CsV_3Sb_5. *Nature* **599**, 216–221 (2021).
19. Chen, Hui et al. Roton pair density wave in a strong-coupling kagome superconductor. *Nature* **599**, 222–228 (2021).
20. Zhou, Y., Kanoda, K. & Ng, T.-K. Quantum spin liquid states. *Rev. Mod. Phys.* **89**, 025003 (2017).
21. Jiang, Y.-X. et al. Unconventional chiral charge order in kagome superconductor KV_3Sb_5. *Nat. Mater.* **20**, 1353–1357 (2021).
22. Mielke, C. et al. Time-reversal symmetry-breaking charge order in a correlated kagome superconductor. *Nature* **602**, 245–250 (2022).
23. Feng, X., Jiang, K., Wang, Z. & Hu, J. Chiral flux phase in the Kagome superconductor AV_3Sb_5. *Sci. Bull.* **66**, 1384–1388 (2021).
24. Denner, M. M., Thomale, R. & Neupert, T. Analysis of charge order in the kagome metal AV_3Sb_5 (A = K, Rb, Cs). *Phys. Rev. Lett.* **127**, 217601 (2021).
25. Lin, Y.-P. & Nandkishore, R. M. Complex charge density waves at van Hove singularity on hexagonal lattices: Haldane-model phase diagram and potential realization in the kagome metals AV_3Sb_5 (A = K, Rb, Cs). *Phys. Rev. B* **104**, 045122 (2021).
26. Park, T., Ye, M. & Balents, L. Electronic instabilities of kagome metals: saddle points and Landau theory. *Phys. Rev. B* **104**, 035142 (2021).
27. Tan, H. et al. Charge density waves and electronic properties of superconducting kagome metals. *Phys. Rev. Lett.* **127**, 046401 (2021).
28. Setty, C., Hu, H. Chen, L. & Si, Q. Electron correlations and *T*-breaking density wave order in a Z_2 kagome metal. Preprint at https://arxiv.org/abs/2105.15204 (2021).
29. Sales, B. C. et al. Tuning the flat bands of the kagome metal CoSn with Fe, In, or Ni doping. *Phys. Rev. Mater.* **5**, 044202 (2021).
30. Li, H. et al. Conjoined charge density waves in the kagome superconductor CV_3Sb_5. *Nat. Commun.* **13**, 6348 (2022).
31. Qian, T. et al. Revealing the competition between charge density wave and superconductivity in CsV_3Sb_5 through uniaxial strain. *Phys. Rev. B* **104**, 144506 (2021).
32. Teng, X. et al. Discovery of charge density wave in a correlated kagome lattice antiferromagnet. *Nature* **609**, 490–495 (2022).
33. Yin, J.-X. et al. Discovery of charge order and corresponding edge state in kagome magnet FeGe. *Phys. Rev. Lett.* **129**, 166401 (2022).
34. Ohoyama, T., Kanematsu, K. & Yasukōchi, K. A new intermetallic compound FeGe. *J. Phys. Soc. Jpn* **18**, 589–589 (1963).
35. Bernhard, J., Lebech, B. & Beckman, O. Neutron diffraction studies of the low-temperature magnetic structure of hexagonal FeGe. *J. Phys. F* **14**, 2379–2393 (1984).
36. Huang, L. & Lu, H. Signatures of Hundness in kagome metals. *Phys. Rev. B* **102**, 125130 (2020).
37. Setty, C. et al. Electron correlations and charge density wave in the topological kagome metal FeGe. Preprint at https://arxiv.org/abs/2203.01930 (2022).
38. Ptok, A. et al. Chiral phonons in the honeycomb sublattice of layered CoSn-like compounds. *Phys. Rev. B* **104**, 054305 (2021).
39. Sobota, J., He, Y. & Shen, Z.-X. Angle-resolved photoemission studies of quantum materials. *Rev. Mod. Phys.* **93**, 025006 (2021).
40. Kang, M. et al. Twofold van Hove singularity and origin of charge order in topological kagome superconductor CsV_3Sb_5. *Nat. Phys.* **18**, 301–308 (2021).
41. Yu, T. L. et al. Colossal band renormalization and Stoner ferromagnetism induce by electron–antiferromagnetic–magnon coupling. *Nat. Commun.* **13**, 6560 (2020).
42. Wray, L. et al. Momentum dependence of superconducting gap, strong-coupling dispersion kink, and tightly bound Cooper pairs in the high-T_c $(Sr,Ba)_{1-x}(K,Na)_xFe_2As_2$ superconductors. *Phys. Rev. B* **78**, 184508 (2008).
43. Grimvall, G. in *Metals* (ed Wohlfarth, E.) (North-Holland, 1981).
44. Plummer, E. W., Shi, J. R., Tang, S. J., Rotenberg, E. & Kevan, S. D. Enhanced electron–phonon coupling at metal surfaces. *Prog. Surf. Sci.* **74**, 251–268 (2003).
45. Luo, H. et al. Electronic nature of charge density wave and electron–phonon coupling in kagome superconductor KV_3Sb_5. *Nat. Commun.* **13**, 273 (2022).
46. Xie, Y. et al. Electron–phonon coupling in the charge density wave state of CsV_3Sb_5. *Phys. Rev. B* **105**, L140501 (2022).
47. Li, H. et al. Observation of unconventional charge density wave without acoustic phonon anomaly in kagome superconductors AV_3Sb_5 (A = Rb, Cs). *Phys. Rev. X* **11**, 031050 (2021).
48. Wu, S. et al. Charge density wave order in kagome metal AV_3Sb_5 (A = Cs, Rb, K). *Phys. Rev. B* **105**, 155106 (2022).
49. Wang, C. et al. Origin of charge density wave in the layered kagome metal CsV_3Sb_5. *Phys. Rev. B* **105**, 045135 (2022).
50. Liu, Z. et al. Charge-density-wave-induced bands renormalization and energy gaps in a kagome superconductor RbV_3Sb_5. *Phys. Rev. X* **11**, 041010 (2021).

Methods

Single crystals were synthesized using chemical vapour transport[32]. ARPES measurements were carried out at BL 5-2 of the Stanford Synchrotron Radiation Lightsource and the MAESTRO beamline (7.0.2) of the Advanced Light Source, with a DA30 electron analyser and an R4000 electron analyser with deflector mode, respectively. FeGe single crystals were cleaved in situ in ultra-high vacuum with a base pressure better than 5×10^{-11} torr. Samples were cleaved in the (001) orientation. Two types of terminations were found, one corresponding to the kagome layer and another to the Ge layer. Both bulk and surface states were identified on both types of terminations. A detailed discussion on the terminations is provided in the Supplementary Information. The data shown in the main text come from the Ge termination unless specifically stated otherwise, but all the features discussed are those that are found in both terminations, hence being representative of the bulk kagome lattice. The energy and angular resolutions used were better than 20 meV and 0.1°, respectively. Measurements shown were taken with a beam spot smaller than 50 μm × 50 μm. All gap measurements were done with correction of the Fermi level by a measurement of polycrystalline gold that was electrically connected to the sample.

INS experiments were carried out on the ARCS (BL-18) spectrometer at the Spallation Neutron Source at Oak Ridge National Laboratory[51] on 0.9 g of co-aligned single-crystal samples. The definition of momentum transfer **Q** in reciprocal space in units of Å^{-1} is given by **Q** = H**a***+K**b***+L**c***, where H, K and L are Miller indices. The direction vectors **a**, **b** and **c** are specified with direction as shown in Fig. 1a,b. The reciprocal lattice vectors **a***, **b*** and **c*** are calculated using **a*** = 2π(**b**×**c**)/[**a**·(**b**×**c**)], **b*** = 2π(**c**×**a**)/[**a**·(**b**×**c**)] and **c*** = 2π(**a**×**b**)/[**a**·(**b**×**c**)]. The scattering plane is [H, H, L]. We measured the neutron spectrum at 120 K, 70 K and 8 K by scanning the angle about the vertical axis by 140° in 1° steps with incident energies of 100 meV (Fig. 5f) and 45 meV (Fig. 5e). Cuts and slices from the **Q**, E data set are extracted using Mantid[52] and Horace[53]. Magnon and phonon spectrum are plotted using low-**Q** ($L = [-2.6, 0]$) and high-**Q** ($L = [-3.1, -2.9]$) data, respectively. The vibration direction of phonons observed by INS is always parallel to the momentum transfer **Q** (Fig. 5g), so the phonon mode shown in Fig. 5e is mostly the A_{2u} mode vibrating along the c axis. Constant-**Q** cuts of the measured phonon spectra are extracted at the Γ (Fig. 5h) and M points (Fig. 5i) and fitted using a Lorentzian and a linear background.

DFT calculations are performed with the Vienna ab initio simulation package[54,55]. The exchange–correlation interaction between electrons is mimicked with the generalized gradient approximation as parameterized by Perdew et al.[56]. A cutoff energy of 350 eV and a **k** mesh of 12 × 12 × 8 are used throughout. Experimental lattice constants are employed, and the atomic positions are fully relaxed until the remaining force is less than 1 meV Å^{-1}. Both the paramagnetic and antiferromagnetic structures are calculated. All calculations are performed considering the spin–orbital coupling, except for the structure relaxation and phonon dispersion calculation. The phonon dispersion is calculated by the finite displacement method as implemented in the PHONONPY software[57]. To calculate the Fermi surface and electron Lindhard susceptibility, we first fitted the DFT band structure with Wannier orbitals (Fe d and Ge p) as implemented in Wannier90 software[58] and then calculate the 3D Fermi surface in the full BZ based on the obtained tight-binding Hamiltonian with a **k** mesh of 150 × 150 × 80. The electron susceptibility is calculated on the basis of the Fermi surface by employing the method described in ref. [59].

Data availability

Source data are provided with this paper. All other data that support the findings of this study are available from the corresponding authors upon reasonable request.

Code availability

The band structure and phonon calculations used in this study are available from the corresponding authors upon reasonable request.

References

51. Abernathy, D. L. et al. Design and operation of the wide angular-range chopper spectrometer ARCS at the Spallation Neutron Source. *Rev. Sci. Instrum.* **83**, 15114 (2012).
52. Arnold, O. et al. Mantid—data analysis and visualization package for neutron scattering and μSR experiments. *Nucl. Instrum.* **764**, 156–166 (2014).
53. Ewings, R. A. et al. Horace: software for the analysis of data from single crystal spectroscopy experiments at time-of-flight neutron instruments. *Nucl. Instrum. Methods Phys. Res. A* **834**, 132 (2016).
54. Kresse, G. & Furthmüller, J. Efficient iterative schemes for ab initio total-energy calculations using a plane-wave basis set. *Phys. Rev. B* **54**, 11169 (1996).
55. Kresse, G. & Furthmüller, J. Efficiency of ab-initio total energy calculations for metals and semiconductors using a plane-wave basis set. *Comput. Mater. Sci.* **6**, 15–50 (1996).
56. Perdew, J. P., Burke, K. & Ernzerhof, M. Generalized gradient approximation made simple. *Phys. Rev. L* **77**, 3865 (1996).
57. Togo, A. & Tanaka, I. First principles phonon calculations in materials science. *Scr. Mater.* **108**, 1 (2015).
58. Mostofi, A. A. et al. wannier90: a tool for obtaining maximally-localised Wannier functions. *Comput. Phys. Commun.* **178**, 685 (2008).
59. Johannes, M. D. & Mazin, I. I. Fermi surface nesting and the origin of charge density waves in metals. *Phys. Rev. B* **77**, 165135 (2008).

Author contributions

M.Y., P.D. and R.J.B. managed the project. The single-crystal FeGe samples were grown by X.T. and B.G. under the guidance of P.D. APRES experiments were carried out by J.S.O., X.T., J.H. and M.Y. with the assistance of M.H., D.L., C.J., A.B. and E.R. First-principles calculations were performed by H.T. and B.Y. Neutron scattering measurements and analysis were carried out by G.G., X.T., L.C. and P.D. The paper was written by M.Y., P.D., X.T., J.S.O. and L.C. with input from and significant discussions with all co-authors.

Competing interests

The authors declare no competing interests.

Additional information